

Bayesian Estimation of White Matter Atlas from High Angular Resolution Diffusion Imaging

Jia Du^a, Alvina Goh^b, Anqi Qiu^{a,c,d,*}

^a*Department of Bioengineering, National University of Singapore, Singapore*

^b*Department of Mathematics, National University of Singapore, Singapore*

^c*Singapore Institute for Clinical Sciences, Agency for Science, Technology and Research, Singapore*

^d*Clinical Imaging Research Center, National University of Singapore, Singapore*

Abstract

We present a Bayesian probabilistic model to estimate the brain white matter atlas from high angular resolution diffusion imaging (HARDI) data. This model incorporates a shape prior of the white matter anatomy and the likelihood of individual observed HARDI datasets. We first assume that the atlas is generated from a known hyperatlas through a flow of diffeomorphisms and its shape prior can be constructed based on the framework of large deformation diffeomorphic metric mapping (LDDMM). LDDMM characterizes a nonlinear diffeomorphic shape space in a linear space of initial momentum uniquely determining diffeomorphic geodesic flows from the hyperatlas. Therefore, the shape prior of the HARDI atlas can be modeled using a centered Gaussian random field (GRF) model of the initial momentum. In order to construct the likelihood of observed HARDI datasets, it is necessary to study the diffeomorphic transformation of individual observations relative to the atlas and the probabilistic distribution of orientation distribution functions (ODFs). To this end, we construct the likelihood related to the transformation using the same construction as discussed for the shape prior of the atlas. The probabilistic distribution of ODFs is then constructed based on the ODF Riemannian manifold. We assume that the observed ODFs are generated by an exponential map of random tangent vectors at the deformed atlas ODF. Hence, the likelihood of the ODFs can be modeled using a GRF of their tangent vectors

*Correspondence to: Anqi Qiu, Department of Bioengineering, National University of Singapore, 9 Engineering Drive 1, Block EA 03-12, Singapore 117576. Tel: +65 6516 7002. Fax: +65 6872 3069

Email address: bieqa@nus.edu.sg (Anqi Qiu)

in the ODF Riemannian manifold. We solve for the maximum a posteriori using the Expectation-Maximization algorithm and derive the corresponding update equations. Finally, we illustrate the HARDI atlas constructed based on a Chinese aging cohort of 94 adults and compare it with that generated by averaging the coefficients of spherical harmonics of the ODF across subjects.

Keywords: Orientation distribution function (ODF), large deformation diffeomorphic metric mapping (LDDMM), Bayesian modeling, white matter atlas.

1. Introduction

The white matter region of the human brain is composed of neuronal axons that provide insights on brain connections. Such information is very useful for identifying neuropathology of mental illnesses and understanding fundamental neuroscience questions on how the brain regions interact each other. Up to now, a comprehensive atlas that well characterizes the *in-vivo* white matter anatomy of the human brain and can be used in atlas-based neuroimaging research remains lacking.

In the last decade, diffusion weighted magnetic resonance imaging (DW-MRI) technique has exploited the property that water molecules move faster along neural axons than against them. By measuring water diffusion in the brain, the location and trajectories of axons can be visualized and the axonal pathways can be reconstructed using DW-MRI. Diffusion tensor imaging (DTI), where axonal orientations are modeled using a three-dimensional ellipsoid tensor, has become one of the most popular mathematical models to study the white matter axonal orientation. DTI has since become a fundamental tool that enables researchers to obtain a deep understanding of the human brain.

There have been several different approaches to DTI atlas construction, either using scalar registration [17, 42], multi-channel methods [33] or by directly optimizing tensor similarity [45]. Since then, a large body of research has leveraged the DTI atlas information. Some of these provided anatomical validation [25] and anatomical labeling of fiber tracts [30, 20]. The comprehensive work by Mori et al. [30] provides a three-dimensional and two-dimensional *in-vivo* atlas of various white matter tracts in the human brain based on DTI and has become an essential resource for neuroimaging researchers. Hua et al. [20] create a white matter parcellation atlas based on probabilistic maps of the major white matter tracts and show that there is an excellent correlation of fractional anisotropy and mean diffusivity between the automated and the individual tractography-based results. Lawes et al. [25] show that it is possible to establish a close correspondence of the fiber tracts generated from the DTI atlas with the tracts isolated with classical dissection of post-mortem brain tissue. A DTI atlas containing the complete diffusion tensor information is constructed by Verhoeven et al. [42]. Using robust fiber tracking methods on this DTI atlas, Verhoeven et al. reconstruct a large number of white matter tracts and show that their framework yields highly reproducible and reliable fiber tracts. de Schotten et al. [10] produce a white matter atlas that describes the *in-vivo* variability of the major association, commissural, and projection connections and study the inter-subject variability between left and right hemispheres in

relation to gender based on this atlas. DTI atlases have been directly used to study white matter fiber tracts [32, 44].

It has been demonstrated that DTI is valuable for studying brain white matter development in children and detecting abnormalities in patients with neuropsychiatric disorders and neurodegenerative diseases [e.g. 22, 27, 35]. However, a major shortcoming of DTI is that it can only reveal one dominant axonal orientation at each location while between one and two thirds of the human brain white matter are thought to contain multiple axonal bundles crossing each other [5]. In contrast, HARDI [41] addresses this well-known limitation of DTI by measuring water diffusion along uniformly distributed directions on the sphere. It can thus characterize more complex axonal geometries. HARDI measurements are used to reconstruct an orientation distribution function (ODF), a probability density function (PDF) defined on the sphere, to describe the axonal distribution. Unlike the tensor model used in DTI, the ODF has no restriction on the number of axons present in a specific anatomical location and thus can well characterize the true underlying white matter architecture. By quantitatively comparing axonal orientations retrieved from the ODFs against histological measurements, Leergaard et al. [26] show that accurate estimates of axon bundles can be obtained from HARDI data, therefore further validating its usage in brain studies.

Over the last decade, atlas generation techniques based on intensity images have matured significantly and they include those based only on affine or non-linear registration methods [24, 4] and probabilistic models coupled to the Expectation-Maximization (EM) algorithm to estimate both a shape prior of the atlas and an intensity image likelihood function [2, 28, 34]. In contrast, the white matter atlas generation based on HARDI is still very much in its infancy. Bouix et al. [7] employ an image registration approach that first seeks the transformation between fractional anisotropic (FA) images and then resample the HARDI signals of each subject into a common coordinate according to this transformation. The HARDI atlas is then generated by averaging the coefficients of spherical harmonics of the ODF across subjects. Yeh and Tseng [43] first construct the spatial normalization of the diffusion information using a q-space diffeomorphic reconstruction method, reconstruct the spin distribution function (SDF) in the ICBM-152 space from the diffusion MR signals, and the white matter atlas is then computed by averaging the SDF over individual subjects. Bloy et al. [6] perform alignment of ODF fields by using a multi-channel diffeomorphic demons registration algorithm on rotationally invariant feature maps and white matter parcellation is done via a spatially coherent normalized cuts algorithms.

To the best of our knowledge, there is no probabilistic framework for generating

the HARDI atlas that incorporates both a shape prior of the white matter anatomy and a probabilistic model of the ODFs. In this paper, we extend the previous Bayesian model for the intensity image atlas generation proposed in [28, 34] to that for HARDI. Briefly, we derive a Bayesian model with a shape prior of the HARDI atlas in terms of diffeomorphic transformations and a likelihood function of the ODFs in terms of their tangent vectors on an ODF Riemannian manifold. As we will see later, the extension of the Bayesian model from intensity images to HARDI is non-trivial. Our main contributions of this work are to construct the likelihood function of the ODFs based on their Riemannian structure and derive the Expectation-Maximization algorithm and the update equations for solving the Bayesian HARDI atlas estimation. In the following methodological sections, we first introduce the general framework of this Bayesian HARDI atlas estimation in §2.1 and construct the shape prior of the atlas and the distribution of random diffeomorphisms given the estimated atlas. In §2.3, we construct the conditional likelihood of ODFs based on their Riemannian manifold. In §2.4, we derive the Expectation-Maximization algorithm to obtain the maximum a posteriori solution and §2.5 gives the proof of the EM update equations. We employ this atlas generation approach on 94 HARDI datasets acquired in a Chinese aging study and §3 illustrates the estimated HARDI atlas. Our findings show that the atlas estimated using our algorithm preserves anatomical details of the white matter. As age increases, the corpus callosum thinning was observed, which is consistent with existing literature, [e.g. 19, 15, 38]. Additionally, we demonstrate age effects on crossing fiber regions. Last but not least, we also compare our method to an existing HARDI atlas generation method by averaging the coefficients of spherical harmonics of the ODF across subjects [6].

2. Methods

2.1. General Framework of Bayesian HARDI Atlas Estimation

In this section, we introduce the general framework of the Bayesian HARDI atlas estimation. Given n observed ODF datasets $J^{(i)}$ for $i = 1, \dots, n$, we assume that each of them can be estimated through an unknown atlas I_{atlas} and a diffeomorphic transformation $\phi^{(i)}$ such that

$$J^{(i)} \approx I^{(i)} = \phi^{(i)} \cdot I_{\text{atlas}}. \quad (1)$$

The total variation of $J^{(i)}$ relative to $I^{(i)}$ is then denoted by σ^2 . The goal here is to estimate the unknown atlas I_{atlas} and the variation σ^2 . To solve for the unknown atlas I_{atlas} , we first introduce an ancillary “hyperatlas” I_0 , and assume that

our atlas is generated from it via a diffeomorphic transformation of ϕ such that $I_{\text{atlas}} = \phi \cdot I_0$. We use the Bayesian strategy to estimate ϕ and σ^2 from the set of observations $J^{(i)}, i = 1, \dots, n$ by computing the maximum a posteriori (MAP) of $f_\sigma(\phi|J^{(1)}, J^{(2)}, \dots, J^{(n)}, I_0)$. This can be achieved using the Expectation-Maximization algorithm by first computing the log-likelihood of the complete data $(\phi, \phi^{(i)}, J^{(i)}, i = 1, 2, \dots, n)$ when $\phi^{(1)}, \dots, \phi^{(n)}$ are introduced as hidden variables. We denote this likelihood as $f_\sigma(\phi, \phi^{(1)}, \dots, \phi^{(n)}, J^{(1)}, \dots, J^{(n)}|I_0)$. We consider that the paired information of individual observations, $(J^{(i)}, \phi^{(i)})$ for $i = 1, \dots, n$, as independent and identically distributed. As a result, this log-likelihood can be written as

$$\begin{aligned} & \log f_\sigma(\phi, \phi^{(1)}, \dots, \phi^{(n)}, J^{(1)}, \dots, J^{(n)}|I_0) \\ &= \log f(\phi|I_0) + \sum_{i=1}^n \left\{ \log f(\phi^{(i)}|\phi, I_0) + \log f_\sigma(J^{(i)}|\phi^{(i)}, \phi, I_0) \right\}, \end{aligned} \quad (2)$$

where $f(\phi|I_0)$ is the shape prior (probability distribution) of the atlas given the hyperatlas, I_0 . $f(\phi^{(i)}|\phi, I_0)$ is the distribution of random diffeomorphisms given the estimated atlas $(\phi \cdot I_0)$. $f_\sigma(J^{(i)}|\phi^{(i)}, \phi, I_0)$ is the conditional likelihood of the ODF data given its corresponding hidden variable $\phi^{(i)}$ and the estimated atlas $(\phi \cdot I_0)$. In the remainder of this section, we first adopt $f(\phi|I_0)$ and $f(\phi^{(i)}|\phi, I_0)$ introduced in [28, 34] and then describe how to calculate $f_\sigma(J^{(i)}|\phi^{(i)}, \phi, I_0)$ in §2.3 based on a Riemannian structure of the ODFs.

2.2. The Shape Prior of the Atlas $f(\phi|I_0)$ and the Distribution of Random Diffeomorphisms $f(\phi^{(i)}|\phi, I_0)$

Adopting previous work [28, 34], we discuss the construction of the shape prior (probability distribution) of the atlas, $f(\phi|I_0)$, under the framework of large deformation diffeomorphic metric mapping (LDDMM, reviewed in Appendix A). By Property 1 in Appendix A, we can compute the prior $f(\phi|I_0)$ via m_0 , i.e.,

$$f(\phi|I_0) = f(m_0|I_0), \quad (3)$$

where m_0 is initial momentum defined in the coordinates of I_0 such that it uniquely determines diffeomorphic geodesic flows from I_0 to the estimated atlas. When I_0 remains fixed, the space of the initial momentum m_0 provides a linear representation of the nonlinear diffeomorphic shape space, I_{atlas} , in which linear statistical analysis can be applied. Hence, assuming m_0 is random, we immediately obtain a stochastic model for *diffeomorphic transformations* of I_0 . More precisely, we follow the work in [28, 34] and make the following assumption.

Assumption 1. (Gaussian Assumption on m_0) m_0 is assumed to be a centered Gaussian random field (GRF) model where the distribution of m_0 is characterized by its covariance bilinear form, defined by

$$\Gamma_{m_0}(v, w) = E[m_0(v)m_0(w)] ,$$

where v, w are vector fields in the Hilbert space of V with reproducing kernel k_V .

We associate Γ_{m_0} with k_V^{-1} . The “prior” of m_0 in this case is then $\frac{1}{\mathcal{Z}} \exp\left(-\frac{1}{2}\langle m_0, k_V m_0 \rangle_2\right)$, where \mathcal{Z} is the normalizing Gaussian constant. This leads to formally define the “log-prior” of m_0 to be

$$\log f(m_0|I_0) \approx -\frac{1}{2}\langle m_0, k_V m_0 \rangle_2 , \quad (4)$$

where we ignore the normalizing constant term $\log \mathcal{Z}$.

We now consider the construction of the distribution of random diffeomorphisms, $f(\phi^{(i)}|\phi, I_0)$. Similar to the construction of the atlas shape prior, we define $f(\phi^{(i)}|\phi, I_0)$ via the corresponding initial momentum $m_0^{(i)}$ defined in the coordinates of $\phi \cdot I_0$. We also assume that $m_0^{(i)}$ is random, and therefore, we again obtain a stochastic model for *diffeomorphic transformations* of $I_{\text{atlas}} \cong \phi \cdot I_0$. We make the following assumption.

Assumption 2. (Gaussian Assumption on $m_0^{(i)}$) $m_0^{(i)}$ is assumed to be a centered GRF model with its covariance as k_V^π , where k_V^π is the reproducing kernel of the smooth vector field in a Hilbert space V .

Hence, we can define the log distribution of random diffeomorphisms as

$$\log f(\phi^{(i)}|\phi, I_0) \approx -\frac{1}{2}\langle m_0^{(i)}, k_V^\pi m_0^{(i)} \rangle_2 . \quad (5)$$

where as before, we ignore the normalizing constant term $\log \mathcal{Z}$.

2.3. The Conditional Likelihood of the ODF Data $f_\sigma(J^{(i)}|\phi^{(i)}, \phi, I_0)$

In this section, we will derive the construction of the conditional likelihood of the ODF data $f_\sigma(J^{(i)}|\phi^{(i)}, \phi, I_0)$. From the field of *information geometry* [3], the space of ODFs, $\mathcal{p}(\mathbf{s})$, forms a Riemannian manifold with the *Fisher-Rao* metric (reviewed in Appendix B). In our study, we choose the square-root representation of the ODFs as the parameterization of the ODF Riemannian manifold, which was

used recently in ODF processing and registration [12, 16, 9]. The *square-root ODF* ($\sqrt{\text{ODF}}$) is defined as $\psi(\mathbf{s}) = \sqrt{p(\mathbf{s})}$, where $\psi(\mathbf{s})$ is assumed to be non-negative to ensure uniqueness. The space of such functions is defined as

$$\Psi = \{\psi : \mathbb{S}^2 \rightarrow \mathbb{R}^+ | \forall \mathbf{s} \in \mathbb{S}^2, \psi(\mathbf{s}) \geq 0; \int_{\mathbf{s} \in \mathbb{S}^2} \psi^2(\mathbf{s}) d\mathbf{s} = 1\}. \quad (6)$$

We refer the interested reader to Appendix B for a more detailed description of the Riemmanian manifold Ψ lies on. It can be shown [37] that the Fisher-Rao metric is simply the \mathbb{L}^2 metric, given as

$$\langle \xi_j, \xi_k \rangle_{\psi_i} = \int_{\mathbf{s} \in \mathbb{S}^2} \xi_j(\mathbf{s}) \xi_k(\mathbf{s}) d\mathbf{s}, \quad (7)$$

where $\xi_j, \xi_k \in T_{\psi_i} \Psi$ are tangent vectors at ψ_i . As we see from the preceding discussion, the ODF image should instead be considered as a function indexed over a unit sphere \mathbb{S}^2 and the image volume $\Omega \subset \mathbb{R}^3$. We denote $J^{(i)}$ as $\psi^{(i)}(\mathbf{s}, x)$, $\mathbf{s} \in \mathbb{S}^2, x \in \Omega$ in the remainder of the paper. Similarly, we have the atlas $I_{\text{atlas}} = \psi_{\text{atlas}}(\mathbf{s}, x)$, where $\psi_{\text{atlas}}(\mathbf{s}, x)$ not only represents the mean anatomical shape characterized through the diffeomorphism but the mean ODF at each spatial location described using $\sqrt{\text{ODF}}$.

Given $\phi_1^{(i)}$ and $\psi_{\text{atlas}}(\mathbf{s}, x)$ at a specific spatial location x , we assume that $\psi^{(i)}(\mathbf{s}, x)$ is generated through an exponential map, i.e., ,

$$\psi^{(i)}(\mathbf{s}, x) = \exp_{\phi_1^{(i)} \cdot \psi_{\text{atlas}}(\mathbf{s}, x)} \left(\xi(x) \right), \quad (8)$$

where the tangent vectors $\xi(x) \in T_{\phi_1^{(i)} \cdot \psi_{\text{atlas}}(\mathbf{s}, x)} \Psi$ lie in a linear space. Therefore, in order to model conditional likelihood of the ODF $f_\sigma(J^{(i)} | \phi^{(i)}, \phi, I_0)$, we make the following assumption.

Assumption 3. (Gaussian Assumption on ξ) $\xi(x) \in T_{\phi_1^{(i)} \cdot \psi_{\text{atlas}}(\mathbf{s}, x)} \Psi$ is assumed to be a centered Gaussian Random Field on the tangent space of Ψ at $\phi_1^{(i)} \cdot \psi_{\text{atlas}}(\mathbf{s}, x)$. In addition, we assume that this Gaussian random field has the covariance as $\sigma^2 \Gamma_{\text{Id}}$.

This assumption is based on previous works on Bayesian atlas estimation using images and shapes [34, 28]. The main difference here is that we assume that $\xi(x) \in T_{\phi_1^{(i)} \cdot \psi_{\text{atlas}}(\mathbf{s}, x)} \Psi$ is assumed to be a centered Gaussian Random Field on the tangent space. We choose Γ_{Id} as the identity operator to be consistent with the inner

product of $\sqrt{\text{ODF}}$ defined in Eq. (7). The group action of the diffeomorphism, $\phi_1^{(i)} \cdot \psi_{\text{atlas}}(\mathbf{s}, x)$, involves both the spatial transformation and reorientation of the ODF. Based on the derivation in our previous work [12], we define this group action as

$$\phi_1^{(i)} \cdot \psi_{\text{atlas}}(\mathbf{s}, x) = \sqrt{\frac{\det(D_{(\phi_1^{(i)})^{-1}\phi_1^{(i)})^{-1}}}{\|(D_{(\phi_1^{(i)})^{-1}\phi_1^{(i)})^{-1}\mathbf{s}\|^3}} \psi_{\text{atlas}}\left(\frac{(D_{(\phi_1^{(i)})^{-1}\phi_1^{(i)})^{-1}\mathbf{s}}{\|(D_{(\phi_1^{(i)})^{-1}\phi_1^{(i)})^{-1}\mathbf{s}\|}, (\phi_1^{(i)})^{-1}(x)\right). \quad (9)$$

This leads to formally define the “log-likelihood” of $\xi(x)$ as

$$-\frac{1}{2\sigma^2} \langle \xi, \xi \rangle_2 = -\frac{1}{2\sigma^2} \left\| \log_{\phi_1^{(i)} \cdot \psi_{\text{atlas}}(\mathbf{s}, x)} \psi^{(i)}(\mathbf{s}, x) \right\|_{\phi_1^{(i)} \cdot \psi_{\text{atlas}}(\mathbf{s}, x)}^2.$$

From the Gaussian assumption, we can thus write the conditional “log-likelihood” of $J^{(i)}$ given I_{atlas} and $\phi_1^{(i)}$ as

$$\begin{aligned} & \log f_{\sigma}(J^{(i)} | \phi_1^{(i)}, \phi_1, I_0) \\ & \approx \int_{x \in \Omega} \left\{ -\frac{1}{2\sigma^2} \left\| \log_{\phi_1^{(i)} \cdot \psi_{\text{atlas}}(\mathbf{s}, x)} \left(\psi^{(i)}(\mathbf{s}, x) \right) \right\|_{\phi_1^{(i)} \cdot \psi_{\text{atlas}}(\mathbf{s}, x)}^2 - \frac{\log \sigma^2}{2} \right\} dx, \end{aligned} \quad (10)$$

where as before, we ignore the normalizing Gaussian term, and I_0 is denoted as $\psi_0(\mathbf{s}, x)$ such that $\psi_{\text{atlas}}(\mathbf{s}, x) = \phi_1 \cdot \psi_0(\mathbf{s}, x)$.

2.4. Expectation-Maximization Algorithm

We have shown how to compute the log-likelihood shown in Eq. (2) in §2.1 and §2.3. In this section, we will show how we employ the Expectation-Maximization algorithm to estimate the atlas, $I_{\text{atlas}} = \psi_{\text{atlas}}(\mathbf{s}, x)$, for $\mathbf{s} \in \mathbb{S}^2, x \in \Omega$, and σ^2 . From the above discussion, we first rewrite the log-likelihood function of the complete data in Eq. (2) as

$$\begin{aligned} & \log f_{\sigma}(\phi, \phi^{(1)}, \dots, \phi^{(n)}, J^{(1)}, \dots, J^{(n)} | I_0) \\ & \approx \log f_{\sigma}(m_0, m_0^{(1)}, \dots, m_0^{(n)}, \psi^{(1)}, \dots, \psi^{(n)} | \psi_0) \\ & \approx -\frac{1}{2} \langle m_0, k_V m_0 \rangle_2 \\ & \quad - \sum_{i=1}^n \left\{ \frac{1}{2} \langle m_0^{(i)}, k_V^{\pi} m_0^{(i)} \rangle_2 + \int_{x \in \Omega} \left\{ \frac{1}{2\sigma^2} \left\| \log_{\phi_1^{(i)} \cdot \psi_{\text{atlas}}(\mathbf{s}, x)} \psi(\mathbf{s}, x) \right\|_{\phi_1^{(i)} \cdot \psi_{\text{atlas}}(\mathbf{s}, x)}^2 + \frac{\log \sigma^2}{2} \right\} dx \right\}, \end{aligned} \quad (11)$$

where $\psi_{\text{atlas}}(\mathbf{s}, x) = \phi_1 \cdot \psi_0(\mathbf{s}, x)$ and can be computed based on Eq. (9).

The E-Step. The E-step computes the expectation of the complete data log-likelihood given the previous atlas m_0^{old} and variance $\sigma^{2\text{old}}$. We denote this expectation as $Q(m_0, \sigma^2 | m_0^{\text{old}}, \sigma^{2\text{old}})$ given in the equation below,

$$\begin{aligned} & Q(m_0, \sigma^2 | m_0^{\text{old}}, \sigma^{2\text{old}}) \tag{12} \\ &= E \left\{ \log f_{\sigma}(m_0, m_0^{(1)}, \dots, m_0^{(n)}, \psi^{(1)}, \dots, \psi^{(n)} | \psi_0) \middle| m_0^{\text{old}}, \sigma^{2\text{old}}, \psi^{(1)}, \dots, \psi^{(n)}, \psi_0 \right\} \\ &\approx -\frac{1}{2} \langle m_0, k_V m_0 \rangle_2 \\ &\quad - \sum_{i=1}^n E \left[\frac{1}{2} \langle m_0^{(i)}, k_V^{\pi} m_0^{(i)} \rangle_2 + \int_{x \in \Omega} \left\{ \frac{1}{2\sigma^2} \left\| \log_{\phi_1^{(i)} \cdot \psi_{\text{atlas}}(\mathbf{s}, x)} \psi^{(i)}(\mathbf{s}, x) \right\|_{\phi_1^{(i)} \cdot \psi_{\text{atlas}}(\mathbf{s}, x)}^2 + \frac{\log \sigma^2}{2} \right\} dx \right]. \end{aligned}$$

The M-Step. The M-step generates the new atlas by maximizing the Q -function with respect to m_0 and σ^2 . The update equation is given as

$$\begin{aligned} & m_0^{\text{new}}, \sigma^{2\text{new}} \tag{13} \\ &= \arg \max_{m_0, \sigma^2} Q(m_0, \sigma^2 | m_0^{\text{old}}, \sigma^{2\text{old}}) \\ &= \arg \min_{m_0, \sigma^2} \left\{ \langle m_0, k_V m_0 \rangle_2 + \sum_{i=1}^n E \left[\int_{x \in \Omega} \left\{ \frac{1}{\sigma^2} \left\| \log_{\phi_1^{(i)} \cdot \psi_{\text{atlas}}(\mathbf{s}, x)} \psi^{(i)}(\mathbf{s}, x) \right\|_{\phi_1^{(i)} \cdot \psi_{\text{atlas}}(\mathbf{s}, x)}^2 + \log \sigma^2 \right\} dx \right] \right\}, \end{aligned}$$

where we use the fact that the conditional expectation of $\langle m_0^{(i)}, k_V^{\pi} m_0^{(i)} \rangle_2$ is constant. We solve σ^2 and m_0 by separating the procedure for updating σ^2 using the current value of m_0 , and then optimizing m_0 using the updated value of σ^2 .

Thus, we can show that it yields the following update equations (the proof is shown later in §2.5),

$$\sigma^{2\text{new}} = \frac{1}{n} \sum_{i=1}^n \int_{x \in \Omega} \left\| \log_{\phi_1^{(i)} \cdot \psi_{\text{atlas}}(\mathbf{s}, x)} \psi^{(i)}(\mathbf{s}, x) \right\|_{\phi_1^{(i)} \cdot \psi_{\text{atlas}}(\mathbf{s}, x)}^2 dx, \tag{14}$$

$$m_0^{\text{new}} = \arg \min_{m_0} \left\{ \langle m_0, k_V m_0 \rangle_2 + \frac{1}{\sigma^{2\text{new}}} \int_{x \in \Omega} \alpha(x) \left\| \log_{\bar{\psi}_0(\mathbf{s}, x)} (\phi_1 \cdot \psi_0(\mathbf{s}, x)) \right\|_{\bar{\psi}_0(\mathbf{s}, x)}^2 dx \right\}, \tag{15}$$

where $\alpha(x) = \sum_{i=1}^n |D\phi_1^{(i)}(x)|$ is a weighted image volume to control the contribution of the HARDI matching errors to the total cost at each voxel level. $|D\phi_1^{(i)}|$ is the Jacobian determinant of $\phi_1^{(i)}$. The mean ODF $\bar{\psi}_0(\mathbf{s}, x)$ is defined as the solution to the following minimization problem

$$\bar{\psi}_0(\mathbf{s}, x) = \arg \min_{\psi \in \Psi} \frac{1}{2} \sum_{i=1}^n \frac{|D\phi_1^{(i)}(x)|}{\sum_{j=1}^n |D\phi_1^{(j)}(x)|} \left\| \log_{\psi(\mathbf{s}, x)} \left((\phi_1^{(i)})^{-1} \cdot \psi^{(i)}(\mathbf{s}, x) \right) \right\|_{\psi(\mathbf{s}, x)}. \quad (16)$$

To compute $\bar{\psi}_0(\mathbf{s}, x)$, the weighed Karcher mean algorithm given in Goh et al. [16] is used. In addition, from Goh et al. [16], we also know that $\bar{\psi}_0(\mathbf{s}, x)$ is the unique solution to

$$\frac{1}{\sum_{j=1}^n |D\phi_1^{(j)}(x)|} \sum_{i=1}^n |D\phi_1^{(i)}(x)| \log_{\bar{\psi}_0(\mathbf{s}, x)} \left((\phi_1^{(i)})^{-1} \cdot \psi^{(i)}(\mathbf{s}, x) \right) = \mathbf{0}. \quad (17)$$

The variational problem listed in Eq. (15) is referred as “modified LDDMM-ODF mapping”, where the weight α is introduced. We now present the steps involved in each iteration in Algorithm 1.

Algorithm 1 (The EM Algorithm for the HARDI Atlas Generation)

We initialize $m_0 = 0$. Thus, the hyperatlas ψ_0 is considered as the initial atlas.

1. Apply the LDDMM-ODF mapping algorithm [12] to register the current atlas to each individual HARDI dataset, which yields $m_0^{(i)}$ and $\phi_t^{(i)}$.
2. Compute $\bar{\psi}_0$ according to Eq. (16) using the weighted Karcher mean algorithm given in Goh et al. [16].
3. Update σ^2 according to Eq. (14).
4. Estimate $\psi_{\text{atlas}} = \phi_1 \cdot \psi_0$, where ϕ_t is found by applying the modified LDDMM-ODF mapping algorithm as given in Eq. (15).

The above computation is repeated until the atlas converges.

2.5. Derivation of update equations of σ^2 and m_0 in EM

We now derive Eqs. (14) and (15) from Q -function in Eq. (12) for updating values of σ^2 and m_0 . It is straightforward to obtain σ^2 by taking the derivative of $Q(m_0, \sigma^2 | m_0^{\text{old}}, \sigma^{2\text{old}})$ with respect to σ^2 and setting it to zero.

For updating m_0 , let $y = \left(\phi_1^{(i)}\right)^{-1}(x)$. By the change of variables strategy, we have

$$\begin{aligned} & \int_{x \in \Omega} \left\| \log_{\phi_1^{(i)} \cdot \psi_{\text{atlas}}(\mathbf{s}, x)} \left(\psi^{(i)}(\mathbf{s}, x) \right) \right\|_{\phi_1^{(i)} \cdot \psi_{\text{atlas}}(\mathbf{s}, x)}^2 dx \\ &= \int_{y \in \Omega} \left\| \log_{\psi_{\text{atlas}}(\mathbf{s}, y)} \left((\phi_1^{(i)})^{-1} \cdot \psi^{(i)}(\mathbf{s}, y) \right) \right\|_{\psi_{\text{atlas}}(\mathbf{s}, y)}^2 |D\phi_1^{(i)}(y)| dy. \end{aligned} \quad (18)$$

Therefore, we can then rewrite

$$\begin{aligned} & \sum_{i=1}^n E \left[\int_{x \in \Omega} \left\{ \frac{1}{2\sigma^2} \left\| \log_{\phi_1^{(i)} \cdot \psi_{\text{atlas}}(\mathbf{s}, x)} \psi^{(i)}(\mathbf{s}, x) \right\|_{\phi_1^{(i)} \cdot \psi_{\text{atlas}}(\mathbf{s}, x)}^2 \right\} dx \right] \\ &= \sum_{i=1}^n E \left[\int_{y \in \Omega} \frac{1}{2\sigma^2} \left\| \log_{\psi_{\text{atlas}}(\mathbf{s}, y)} \left((\phi_1^{(i)})^{-1} \cdot \psi^{(i)}(\mathbf{s}, y) \right) \right\|_{\psi_{\text{atlas}}(\mathbf{s}, y)}^2 |D\phi_1^{(i)}(y)| dy \right] \\ &= \int_{y \in \Omega} \frac{1}{2\sigma^2} \sum_{i=1}^n E \left[\left\| \log_{\psi_{\text{atlas}}(\mathbf{s}, y)} \left((\phi_1^{(i)})^{-1} \cdot \psi^{(i)}(\mathbf{s}, y) \right) \right\|_{\psi_{\text{atlas}}(\mathbf{s}, y)}^2 |D\phi_1^{(i)}(y)| \right] dy \\ &\stackrel{(a)}{\approx} \int_{y \in \Omega} \frac{1}{2\sigma^2} \sum_{i=1}^n E \left[\left\| \log_{\bar{\psi}_0(\mathbf{s}, y)} \left((\phi_1^{(i)})^{-1} \cdot \psi^{(i)}(\mathbf{s}, y) \right) - \log_{\bar{\psi}_0(\mathbf{s}, y)} \left(\psi_{\text{atlas}}(\mathbf{s}, y) \right) \right\|_{\bar{\psi}_0(\mathbf{s}, y)}^2 |D\phi_1^{(i)}(y)| \right] dy \\ &= \int_{y \in \Omega} \frac{1}{2\sigma^2} \sum_{i=1}^n E \left[\left\{ \left\| \log_{\bar{\psi}_0(\mathbf{s}, y)} \left((\phi_1^{(i)})^{-1} \cdot \psi^{(i)}(\mathbf{s}, y) \right) \right\|_{\bar{\psi}_0(\mathbf{s}, y)}^2 + \left\| \log_{\bar{\psi}_0(\mathbf{s}, y)} \left(\psi_{\text{atlas}}(\mathbf{s}, y) \right) \right\|_{\bar{\psi}_0(\mathbf{s}, y)}^2 \right. \right. \\ &\quad \left. \left. - 2 \left\langle \log_{\bar{\psi}_0(\mathbf{s}, y)} \left((\phi_1^{(i)})^{-1} \cdot \psi^{(i)}(\mathbf{s}, y) \right), \log_{\bar{\psi}_0(\mathbf{s}, y)} \left(\psi_{\text{atlas}}(\mathbf{s}, y) \right) \right\rangle_{\bar{\psi}_0(\mathbf{s}, y)} \right\} |D\phi_1^{(i)}(y)| \right] dy \end{aligned}$$

where (a) is the first order approximation of $\left\| \log_{\psi_{\text{atlas}}(\mathbf{s}, y)} \left((\phi_1^{(i)})^{-1} \cdot \psi^{(i)}(\mathbf{s}, y) \right) \right\|_{\psi_{\text{atlas}}(\mathbf{s}, y)}^2$.

As the direct consequence of the Karcher mean definition of $\bar{\psi}_0(\mathbf{s}, y)$ in Eq. (16), and more precisely Eq. (17), $\sum_{i=1}^n |D\phi_1^{(i)}(x)| \log_{\bar{\psi}_0(\mathbf{s}, x)} \left((\phi_1^{(i)})^{-1} \cdot \psi^{(i)}(\mathbf{s}, x) \right) = 0$, the above cross item is equal to zero. Therefore, we get

$$\begin{aligned} & \int_{y \in \Omega} \frac{1}{2\sigma^2} \sum_{i=1}^n E \left[\left\{ \left\| \log_{\bar{\psi}_0(\mathbf{s}, y)} \left((\phi_1^{(i)})^{-1} \cdot \psi^{(i)}(\mathbf{s}, y) \right) \right\|_{\bar{\psi}_0(\mathbf{s}, y)}^2 \right. \right. \\ &\quad \left. \left. + \left\| \log_{\bar{\psi}_0(\mathbf{s}, y)} \left(\psi_{\text{atlas}}(\mathbf{s}, y) \right) \right\|_{\bar{\psi}_0(\mathbf{s}, y)}^2 \right\} |D\phi_1^{(i)}(y)| \right] dy. \end{aligned}$$

Since the first item in the above equation is independent of m_0 , we have

$$m_0^{\text{new}} = \arg \min_{m_0} \langle m_0, k_V m_0 \rangle_2 + \frac{1}{\sigma_{2\text{new}}} \int_{y \in \Omega} \alpha(y) \left\| \log_{\bar{\psi}_0(\mathbf{s}, y)} \left(\phi_1 \cdot \psi_0(\mathbf{s}, y) \right) \right\|_{\bar{\psi}_0(\mathbf{s}, y)}^2 dy ,$$

where $\alpha(y) = \sum_{i=1}^n |D\phi_1^{(i)}(y)|$. By changing y by x , we obtain Eq. (14).

3. Results

In this section, we demonstrate the performance of the probabilistic HARDI atlas generation algorithm proposed on real human data. In §3.1, we show the HARDI atlas based on 94 healthy adults. §3.2 empirically examines the convergence of the HARDI atlas estimation procedure and studies the effects of the choice of the hyperatlas, which is used as the initial atlas in Algorithm 1, on the final estimated atlas. §3.3 shows the estimated atlases across different age groups. Finally, §3.4 compares our proposed algorithm to an existing algorithm in Bloy et al. [6].

Subjects and Image Acquisition: 94 participants were recruited through advertisements posted at the National University of Singapore (NUS). 38 males and 56 females ranged from 22 to 71 years old (mean \pm standard deviation (SD): 42.5 ± 13.9 years) participated in the study. A health screening questionnaire along with informed consent approved by the NUS Institutional Review Board was acquired from each participant. Any participant with a history of psychological, neurological disorder or surgical implantation was excluded from the study. A Mini Mental Status Examination (MMSE) was administered to each participant to rule out possible cognitive impairments. All participants had the MMSE score greater than 26.

Every participant underwent magnetic resonance imaging scans that were performed on a 3T Siemens Magnetom Trio Tim scanner using a 32-channel head coil at Clinical Imaging Research Center at the NUS. The image protocols were: (i) isotropic high angular resolution diffusion imaging (single-shot echo-planar sequence; 48 slices of 3mm thickness; with no inter-slice gaps; matrix: 96×96 ; field of view: 256×256 mm; repetition time: 6800 ms; echo time: 85 ms; flip angle: 90° ; 91 diffusion weighted images (DWIs) with $b = 1150$ s/mm², 11 baseline images without diffusion weighting); (ii) isotropic T2-weighted imaging protocol (spin echo sequence; 48 slices with 3 mm slice thickness; no inter-slice gaps; matrix: 96×96 ; field of view: 256×256 mm; repetition time: 2600 ms; echo time: 99 ms; flip angle: 150°).

HARDI Preprocessing: DWIs of each subject were first corrected for motion and eddy current distortions using affine transformation to the image without diffusion weighting. Within-subject, we followed the procedure detailed in Huang et al. [21] to correct geometric distortion of the DWIs due to b0-susceptibility differences over the brain. Briefly reviewing, the T2-weighted image was considered as the anatomical reference. The deformation that carried the baseline image without diffusion weighting to the T2-weighted image characterized the geometric distortion of the DWI. For this, intra-subject registration was first performed using FLIRT [23] to remove linear transformation (rotation and translation) between the diffusion weighted images and T2-weighted image. Then, LDDMM [13] sought the optimal nonlinear transformation that deformed the baseline image without the diffusion weighting to the T2-weighted image. This diffeomorphic transformation was then applied to every diffusion weighted image in order to correct the nonlinear geometric distortion. Existing literature [39, 11] have proposed different ways of reorienting the diffusion gradients. In this paper, the diffusion gradients are reoriented using the method proposed in Dhollander et al. [11]. Briefly speaking, if ϕ is the diffeomorphism, then the local affine transformation A_x at spatial coordinates x is defined as the Jacobian matrix of ϕ evaluated at x . If \mathbf{g}_i is the i^{th} diffusion gradient, then the reoriented diffusion gradient after the affine transformation A_x is simply $\frac{A_x^{-T} \mathbf{g}_i}{\|A_x^{-T} \mathbf{g}_i\|}$. Finally, we estimated the ODFs using the approach considering the solid angle constraint based on DWI images proposed in Aganj et al. [1].

3.1. HARDI Atlas Generation

To initialize the HARDI atlas generation process, we chose the HARDI dataset of one participant (male, 43 years old) as hyperatlas and assumed $m_0 = 0$ such that the hyperatlas was used as the initial atlas. We then followed Algorithm 1 and ten iterations were repeated. Notice that k_V associated with the covariance of m_0 and k_V^π associated with the covariance of $m_0^{(i)}$ were assumed to be known and predetermined. Since we were dealing with vector fields in \mathbb{R}^3 , the kernel of V is a matrix kernel operator in order to get a proper definition. Making an abuse of notation, we defined k_V and k_V^π respectively as $k_V \text{Id}_{3 \times 3}$ and $k_V^\pi \text{Id}_{3 \times 3}$, where $\text{Id}_{3 \times 3}$ is a 3×3 identity matrix and k_V and k_V^π are scalars. In particular, we assumed that k_V and k_V^π are Gaussian with kernel sizes of σ_V and σ_{V^π} . Since σ_V determines the smoothness level of the mapping from the hyperatlas to the blur $\bar{\psi}_0(\mathbf{s}, x)$ whereas σ_{V^π} determines that from the sharp atlas to individual HARDI datasets, σ_V should be greater than σ_{V^π} . We experimentally determined $\sigma_{V^\pi} = 5$ and $\sigma_V = 8$.

Figure 1 shows the evolution of $\bar{\psi}_0(s, x)$ over the iterations of the EM algorithm. As seen in Figure 1, the white matter anatomy of $\bar{\psi}_0(s, x)$ was blur at the initial estimate and became sharper as more iterations were run. The computational time for each LDDMM-ODF mapping was about 30 minutes. Figure ?? illustrates the atlas estimated from the 94 adults' HARDI datasets after ten iterations. Panels (a-c) shows the coronal view of the atlas, while panels (d-f) and (g-i) respectively illustrate the axial and sagittal views of the atlas. Figure 2 shows the branching and crossing bundles in the estimated atlases over the entire population group, suggesting that the atlas preserves the anatomical details of the white matter.

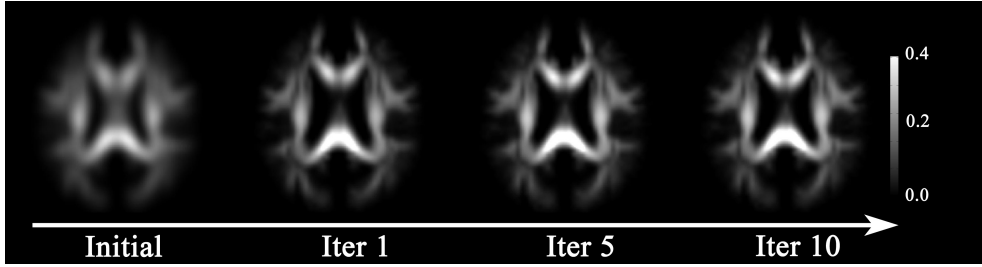


Figure 1: The evolution of $\bar{\psi}_0(s, x)$ over the optimization of the atlas estimation. Panels from left to right show $\bar{\psi}_0(s, x)$ before the optimization, at the first, fifth, and tenth iterations, respectively. The intensity indicates the $\sqrt{\text{ODF}}$ metric of each voxel with respect to the spherical ODF. The larger the value, the more anisotropic the ODF is.

3.2. Convergence and Effects of Hyperatlas Choice of the HARDI Atlas Estimation

In this section, we empirically demonstrate the convergence of the average diffeomorphic metric of individual subjects when referenced to the estimated atlas. This is measured using the square root of the inner product of the initial momentum. Figure 3 shows the evolution of the average diffeomorphic metric of individual subjects referenced to the estimated atlas as well as the standard deviation across the subjects. From Figure 3, we see that the average diffeomorphic metric changed less than 5% after two iterations.

Next, we study the effects of the hyperatlas choice on the estimated atlas. In the Bayesian modeling for the HARDI atlas generation presented here, the hyperatlas ψ_0 is assumed to be known and fixed. In addition, the hyperatlas is used as the initialization for the atlas in the EM algorithm. Therefore, the anatomy of the estimated atlas can be dependent on the choice of the hyperatlas. In this section, we demonstrate the influence due to the hyperatlas.

We repeated the atlas estimation procedure when two different HARDI datasets, shown in Figure 4 (a, c), are respectively used as the hyperatlas. In this experiment, instead of using the entire dataset of 94 adults, only ten HARDI datasets were chosen from our sample pool as the observables, $\psi^{(i)}$, $i = 1, 2, \dots, 10$. Figure 4 (b, d) show the estimated HARDI atlases obtained from the hyperatlases shown in Figure 4 (a, c), respectively. As seen in Figure 4 (e), differences between the two hyperatlases are large in terms of the $\sqrt{\text{ODF}}$ metric square even in major white matter bundles (e.g., corpus callosum, external capsule). Nevertheless, Figure 4 (f), which shows the $\sqrt{\text{ODF}}$ metric square between the estimated two atlases, illustrates that they are similar. A two-sample Kolmogorov-Smirnov test revealed that the cumulative distribution of the $\sqrt{\text{ODF}}$ metric square as shown in Figure 5 between the two estimated atlases (Figure 4 (b, d)) is significantly greater than that between the two hyperatlases (Figure 4 (a, c)) ($p < 0.001$), which indicates that more voxels with small $\sqrt{\text{ODF}}$ between the two estimated atlases when compared to those between the two hyperatlases. This result suggests that the choice of the hyperatlas has minimal effects on the resulting estimated atlas.

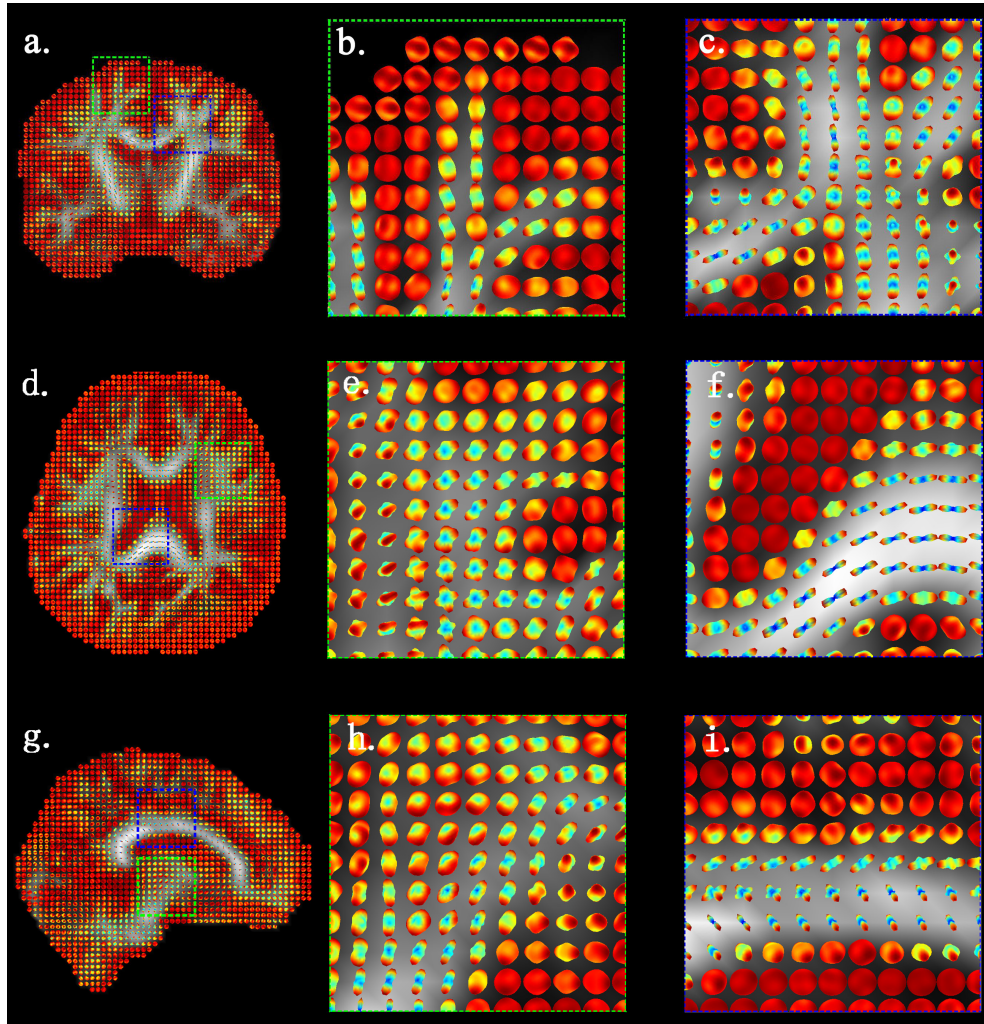


Figure 2: Illustration of the branching and crossing bundles in the estimated atlases over the entire population group. Panels (a,d,g) show the ODF field in the coronal, axial, and sagittal views. In each row, the second and third panels show two zoom-in regions for branching and crossing bundles corresponding to the anatomy on the first panel.

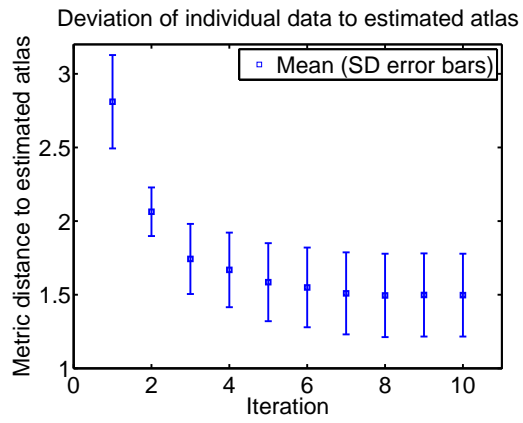


Figure 3: The evolution of the average diffeomorphic metric between individual subjects and the estimated atlas, with the standard deviation shown by the error bars.

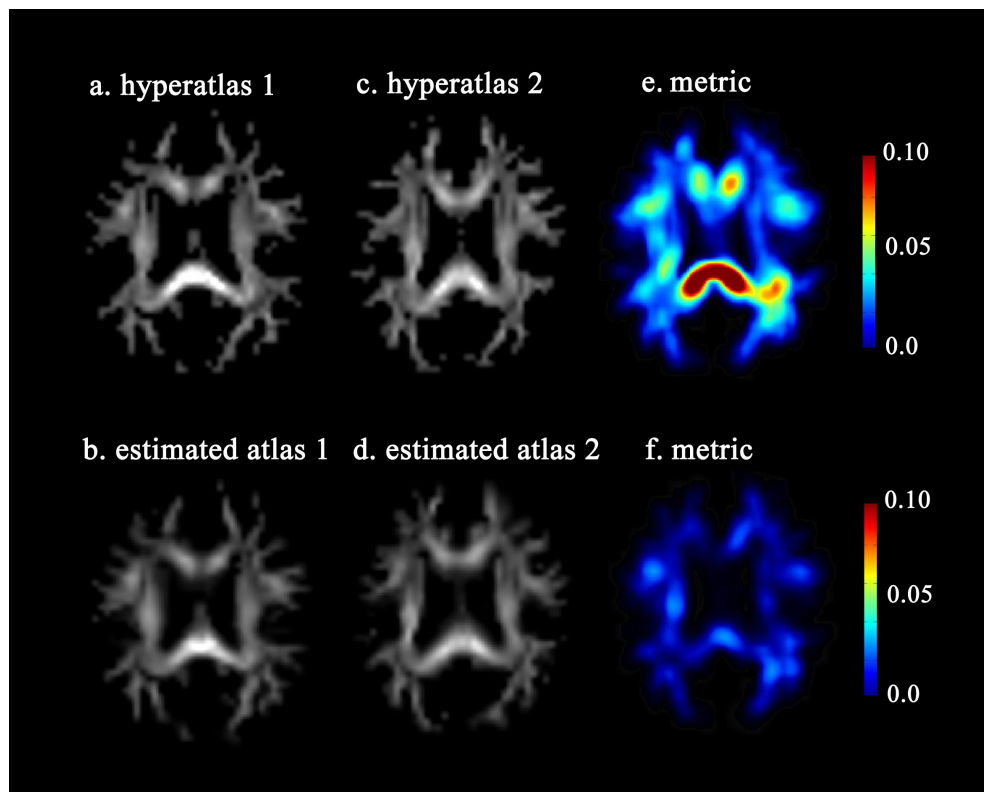


Figure 4: Influences of the hyperatlas on the estimated atlas. Two HARDI datasets (panels (a, c)) were respectively used as the hyperatlas in the Bayesian atlas estimation, which generated the atlases shown in panels (b, d). Panel (e) shows the $\sqrt{\text{ODF}}$ metric square between the two hyperatlases on (a, c), while panel (f) shows that between the atlases on (b, d).

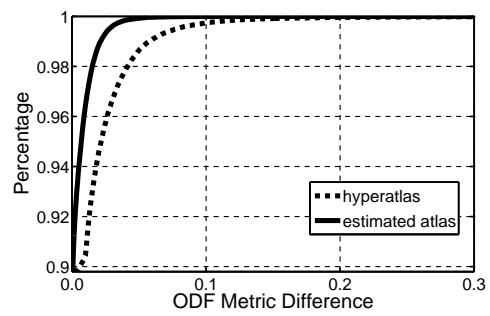


Figure 5: The cumulative distributions of the $\sqrt{\text{ODF}}$ metric square between the two hyperatlases (Figure 4 (a, c)) and between the two estimated atlases (Figure 4 (b, d)) are respectively shown in the dashed and solid lines.

3.3. Aging HARDI atlases

In this section, we performed our HARDI atlas generation process on two different age groups, young and old adults, and demonstrated that the estimated atlas of each specific age group exhibits characteristics of the group that are in line with what is reported in current literature.

We selected a subset of the dataset and divided them into two groups. In the young adults group, there were 21 subjects (8 males and 13 females) ranging from 22 to 39 years old (mean \pm standard deviation (SD): 27.6 ± 4.28 years); In the old adults group, there were also 21 subjects (9 males and 12 females) ranging from 55 to 71 years old (mean \pm standard deviation (SD): 61.90 ± 3.81 years). Next, we choose one subject (male, 24 years old) as the hyperatlas for the young adults group and another subject (male, 71 years old) for the old adults group, and performed the proposed atlas generation algorithm shown in Algorithm 1 for each of the two groups.

In Figure 6, three regions of interest are selected for comparison between the atlases for young and old adults groups. For the regions of the corpus callosum and ventricles in panels (c, g), the most obvious aging effect observed is the bending of the corpus callosum due to the enlargement of ventricles, together with the thinning of the corpus callosum, which is consistent with previous findings in [19, 15, 38]. For the region of the branching fibers, panels (b, f) show that there are more branches in the atlas of young adults group than those in the one of old adults group. The similar effect is also observed in the region of the crossing fibers in panels (d, h). A detailed comparison of the ODF shape explains that the anisotropy for the ODFs declines with advancing age due to the fact that axons' distribution becomes more uniform as age increases. This ODF shape differences could be due to the breakdown of the myelin sheath with aging and increases in extracellular fluid and transverse diffusivity as suggested in Moseley [31].

3.4. Comparison with existing method

In this section, we compared our proposed method with the one proposed in Bloy et al. [6]. In the rest of this section, we referred the atlas generated from our proposed method as *Bayesian* atlas, and the one from Bloy et al. [6] as *averaged* atlas. While the code used in Bloy et al. [6] is not publicly available, we manage to adapt it into the same LDDMM framework as our proposed method. To implement the ODF-based registration algorithm in Bloy et al. [6], we minimized the mean square error (MSE) of the spherical harmonic coefficients (SHC) of ODFs between the warped atlas and subjects, and then applied the finite strain scheme, which only keeps the rotation part of the local Jacobian field, to reorientate the ODFs.

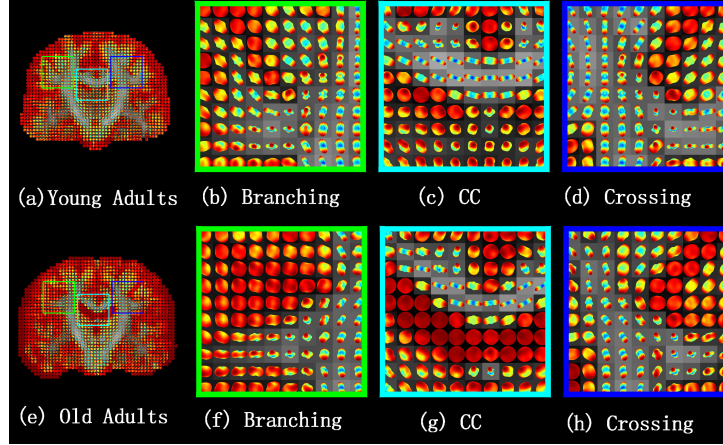


Figure 6: Comparison of HARDI atlases respectively generated from young and old adults. In each row, the last three columns show three zoom-in regions for branching and crossing bundles corresponding to the anatomy given on the first panel.

To generate an average atlas for the dataset, we first selected the same subject as the hyperatlas, and warped each subject into the hyperatlas space using by the registration method we describe above. Finally, we generated the average atlas by averaging the SHC across all the warped subjects. For a fair comparison, we kept all other conditions the same for the generation of both *Bayesian* and *averaged* atlases, and conducted the experiments by selecting the same hyperatlas for the entire dataset.

As shown in Figure 7, the ODFs in the *Bayesian* atlas is generally much sharper than those in the *averaged* atlas. Moreover, as demonstrated in panels (b, f), some small branches can only be revealed in the *Bayesian* atlas, while they cannot be found in the *averaged* atlas due to the averaging process. Furthermore, in the region of crossing fibers shown in panels (c, g), the *Bayesian* atlas preserved more details than the *averaged* atlas. However, there was not much difference in the main fiber tract as illustrated in panels (d, h).

4. Conclusion

In this paper, we present a Bayesian model to estimate the white matter atlas from observed HARDI datasets under the LDDMM framework. To the best of our knowledge, this is the first probabilistic approach for the HARDI atlas generation.

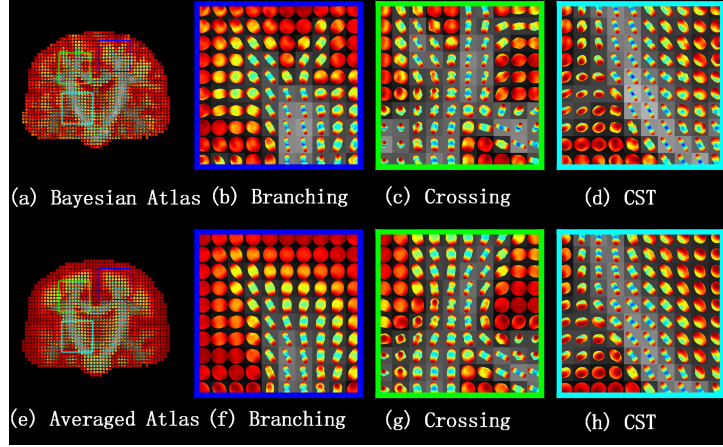


Figure 7: Comparison between Bayesian and averaged atlases. In each row, the last three columns show three zoom-in regions for branching and crossing bundles corresponding to the anatomy given on the first panel.

In this work, we construct the ODF likelihood function based on its Riemannian structure. In particular, we employ the square root parameterization of the ODF Riemannian manifold such that the logarithmic and exponential maps are in closed forms. This facilitates the construction of the ODF likelihood through the tangent vector of the ODF, i.e., logarithmic map, lying in a linear space where linear statistical models can be applied. We further derive the EM algorithm for solving this atlas generation problem. We empirically demonstrate the convergence of this algorithm in terms of both diffeomorphic metric and the ODF metric and show that the estimated atlas has little influence from the hyperatlas. The comparison with the existing algorithm in Bloy et al. [6] showed that our algorithm preserves sharpness of cross and branch fibers. Hence, this atlas generated using our approach will be valuable for population-based studies based on HARDI.

Acknowledgments

The work reported here was supported by grants A*STAR SICS-09/1/1/001, a centre grant from the National Medical Research Council (NMRC/CG/NUHS/2010), the Young Investigator Award at National University of Singapore (NUSYIA FY10 P07), and National University of Singapore MOE AcRF Tier 1.

Appendix A: The Shape Prior of the Atlas $f(\phi|I_0)$ and the Distribution of Random Diffeomorphisms $f(\phi^{(i)}|\phi, I_0)$

Adopting previous work [28, 34], we will first derive the construction of the shape prior (probability distribution) of the atlas, $f(\phi|I_0)$, and the distribution of random diffeomorphisms $f(\phi^{(i)}|\phi, I_0)$, by first reviewing the framework of large deformation diffeomorphic metric mapping (LDDMM). We will then show how one would define the shape prior via the initial momentum m_0 in LDDMM. Finally, using the same construction as in the case of the shape prior, we illustrate the construction of the distribution of the random diffeomorphisms $f(\phi^{(i)}|\phi, I_0)$.

In LDDMM, we assume that the atlas I_{atlas} is constructed as an orbit of I_0 under the group of diffeomorphic transformations \mathcal{G} , i.e., $\mathcal{I}_{\text{atlas}} = \mathcal{G} \cdot I_0$. The diffeomorphic transformations are introduced as transformations of the coordinates on the background space $\Omega \subset \mathbb{R}^3$, i.e., $\mathcal{G} : \Omega \rightarrow \Omega$. One approach, proposed by Grenander and Miller [18] and adopted in this paper, is to construct diffeomorphisms $\phi_t \in \mathcal{G}$ as a geodesic flow generated via ordinary differential equations (ODEs), where $\phi_t, t \in [0, 1]$ obeys the following equation,

$$\dot{\phi}_t = v_t(\phi_t), \quad \phi_0 = \text{Id}, \quad t \in [0, 1], \quad (4-19)$$

where Id denotes the identity map and v_t are the associated velocity vector fields. The vector fields v_t are constrained to be sufficiently smooth, so that Eq. (4-19) is integrable and generates diffeomorphic transformations over finite time. The smoothness is ensured by forcing v_t to lie in a smooth Hilbert space $(V, \|\cdot\|_V)$ with s -derivatives having finite integral square and zero boundary [14, 40]. In our case, we model V as a reproducing kernel Hilbert space with a linear operator L associated with the norm square $\|u\|_V^2 = \langle Lu, u \rangle_2$, where $\langle \cdot, \cdot \rangle_2$ denotes the \mathbb{L}^2 inner product. The group of diffeomorphisms $\mathcal{G}(V)$ are the solutions of Eq. (4-19) with the vector fields satisfying $\int_0^1 \|v_t\|_V dt < \infty$. Thus, this geodesic $\phi_t, t \in [0, 1]$ which lies in the manifold of diffeomorphisms generates I_{atlas} from I_0 , is defined as

$$\phi_0 = \text{Id}, \quad \phi_1 \cdot I_0 = I_{\text{atlas}}.$$

The length of this geodesic is then defined as the Riemannian length of ϕ_t , computed as the integral of the norm of the vector field $\|v_t\|_V$ associated with ϕ_t . Alternatively, by using the duality isometry in Hilbert spaces, one can show that this geodesic length can be equivalently expressed in terms of the momentum m_t . m_t is defined as a linear transformation of v_t through kernel $k_V = L^{-1}$ associated with the reproducing kernel Hilbert space V . More precisely, k_V maps v_t to m_t , i.e.,

$k_V : v_t \rightarrow m_t = k_V^{-1}v_t$. Therefore, for any $u \in V$, $\langle m_t, u \rangle_2 = \langle k_V^{-1}v_t, u \rangle_2$, where $\langle \cdot, \cdot \rangle_2$ denote the \mathbb{L}^2 inner product. One can prove that m_t satisfies the following property at all times [29].

Conservation Law of Momentum. For all $u \in V$,

$$\langle m_t, u \rangle_2 = \langle m_0, (D\phi_t)^{-1}u(\phi_t) \rangle_2. \quad (4-20)$$

Eq. (4-20) uniquely specifies m_t as a linear form on V , given the initial momentum m_0 and the evolving diffeomorphism ϕ_t . We see that by making a change of variables and obtain the following expression relating m_t to the initial momentum m_0 and the geodesic ϕ_t connecting I_0 and I_{atlas} ,

$$m_t = |D\phi_t^{-1}|(D\phi_t^{-1})^\top m_0 \circ \phi_t^{-1}. \quad (4-21)$$

As a direct consequence of this property, given the initial momentum m_0 , one can generate a unique time-dependent diffeomorphic transformation. As a result of the preceding discussion, the following property holds true.

Property 1. When I_0 remains fixed, the space of the initial momentum m_0 provides a linear representation of the nonlinear diffeomorphic shape space, I_{atlas} , in which linear statistical analysis can be applied.

Appendix B: Riemannian Manifold of Square-Root ODF

The ODF is a PDF defined on a unit sphere \mathbb{S}^2 and its space is defined as

$$\mathcal{P} = \{p : \mathbb{S}^2 \rightarrow \mathbb{R}^+ | \forall s \in \mathbb{S}^2, p(s) \geq 0; \int_{s \in \mathbb{S}^2} p(s) ds = 1\}.$$

The space of p forms a Riemannian manifold, also known as the statistical manifold, which is well-known from the field of *information geometry* [3]. Rao [36] introduced the notion of the statistical manifold whose elements are probability density functions and composed the Riemannian structure with the *Fisher-Rao* metric. Cencov [8] showed that the Fisher-Rao metric is the *unique intrinsic metric* on the statistical manifold \mathcal{P} and therefore invariant to re-parameterizations of the functions. There are many different parameterizations of PDFs that are equivalent but with different forms of the Fisher-Rao metric, leading to the Riemannian operations with different computational complexity. In our study, we choose the square-root representation, which was used recently in ODF processing and registration [12, 16, 9]. The square-root representation is one of the most

efficient representations found to date as the various Riemannian operations, such as geodesics, exponential maps, and logarithm maps, are available in closed form.

The *square-root ODF* ($\sqrt{\text{ODF}}$) is defined as $\psi(\mathbf{s}) = \sqrt{p(\mathbf{s})}$, where $\psi(\mathbf{s})$ is assumed to be non-negative to ensure uniqueness. The space of such functions is defined as

$$\Psi = \{\psi : \mathbb{S}^2 \rightarrow \mathbb{R}^+ | \forall \mathbf{s} \in \mathbb{S}^2, \psi(\mathbf{s}) \geq 0; \int_{\mathbf{s} \in \mathbb{S}^2} \psi^2(\mathbf{s}) d\mathbf{s} = 1\}.$$

We see that the functions ψ lie on the positive orthant of a unit Hilbert sphere, a well-studied Riemannian manifold. It can be shown [37] that the Fisher-Rao metric is simply the \mathbb{L}^2 metric, given as

$$\langle \xi_j, \xi_k \rangle_{\psi_i} = \int_{\mathbf{s} \in \mathbb{S}^2} \xi_j(\mathbf{s}) \xi_k(\mathbf{s}) d\mathbf{s},$$

where $\xi_j, \xi_k \in T_{\psi_i} \Psi$ are tangent vectors at ψ_i . The geodesic distance between any two functions $\psi_i, \psi_j \in \Psi$ on a unit Hilbert sphere is the angle

$$\text{dist}(\psi_i, \psi_j) = \|\log_{\psi_i}(\psi_j)\|_{\psi_i} = \cos^{-1} \langle \psi_i, \psi_j \rangle = \cos^{-1} \left(\int_{\mathbf{s} \in \mathbb{S}^2} \psi_i(\mathbf{s}) \psi_j(\mathbf{s}) d\mathbf{s} \right), \quad (4-22)$$

where $\langle \cdot, \cdot \rangle$ is the normal dot product between points in the sphere under the \mathbb{L}^2 metric. For the sphere, the *exponential map* has the closed-form formula

$$\exp_{\psi_i}(\xi) = \cos(\|\xi\|_{\psi_i}) \psi_i + \sin(\|\xi\|_{\psi_i}) \frac{\xi}{\|\xi\|_{\psi_i}},$$

where $\xi \in T_{\psi_i} \Psi$ is a tangent vector at ψ_i and $\|\xi\|_{\psi_i} = \sqrt{\langle \xi, \xi \rangle_{\psi_i}}$. By restricting $\|\xi\|_{\psi_i} \in [0, \frac{\pi}{2}]$, we ensure that the exponential map is bijective. The *logarithm map* from ψ_i to ψ_j has the closed-form formula

$$\overrightarrow{\psi_i \psi_j} = \log_{\psi_i}(\psi_j) = \frac{\psi_j - \langle \psi_i, \psi_j \rangle \psi_i}{\sqrt{1 - \langle \psi_i, \psi_j \rangle^2}} \cos^{-1} \langle \psi_i, \psi_j \rangle.$$

References

References

- [1] Aganj, I., Lenglet, C., Sapiro, G., Yacoub, E., Ugurbil, K., Harel, N., 2010. Reconstruction of the orientation distribution function in single- and multiple-shell q-ball imaging within constant solid angle. *MRM* 64, 554–566.

- [2] Allasonnière, S., Amit, Y., Trouvé, A., 2007. Towards a coherent statistical framework for dense deformable template estimation. *Journal Of The Royal Statistical Society Series B* 69 (1), 3–29.
- [3] Amari, S., 1985. *Differential-Geometrical Methods in Statistics*. Springer.
- [4] Avants, B., Gee, J. C., 2004. Geodesic estimation for large deformation anatomical shape and intensity averaging. *NeuroImage* 23, 139–150.
- [5] Behrens, T., Berg, H. J., Jbabdi, S., Rushworth, M., Woolrich, M., 2007. Probabilistic diffusion tractography with multiple fibre orientations: What can we gain? *NeuroImage* 34 (1), 144–155.
- [6] Bloy, L., Ingallhalikar, M., Eavani, H., Schultz, R. T., Roberts, T. P., Verma, R., 2011. White matter atlas generation using HARDI based automated parcellation. *NeuroImage*.
- [7] Bouix, S., Rathi, Y., Sabuncu, M., 2010. Building an average population hardi atlas. *Information MICCAI 2010 Workshop on Computational Diffusion MRI*.
- [8] Cencov, N. N., 1982. Statistical decision rules and optimal inference. In: *Translations of Mathematical Monographs*. Vol. 53. AMS.
- [9] Cheng, J., Ghosh, A., Jiang, T., Deriche, R., 2009. A Riemannian framework for orientation distribution function computing. In: *MICCAI*. pp. 911–918.
- [10] de Schotten, M. T., ffytche, D. H., Bizzi, A., Dell’Acqua, F., Allin, M., Walshe, M., Murray, R., Williams, S. C., Murphy, D. G., Catani, M., 2011. Atlasing location, asymmetry and inter-subject variability of white matter tracts in the human brain with MR diffusion tractography. *NeuroImage* 54 (1), 49 – 59.
- [11] Dhollander, T., Hecke, W. V., Maes, F., Suetens, S. S. P., 2010. Spatial transformations of high angular resolution diffusion imaging data in Q-space. In: *MICCAI WORKSHOP ON COMPUTATIONAL DIFFUSION MRI*.
- [12] Du, J., Goh, A., Qiu, A., 2011. Diffeomorphic metric mapping of high angular resolution diffusion imaging based on riemannian structure of orientation distribution functions. *IEEE Trans. on Medical Imaging*.
- [13] Du, J., Younes, L., Qiu, A., 2011. Whole brain diffeomorphic metric mapping via integration of sulcal and gyral curves, cortical surfaces, and images. *NeuroImage* 56 (1), 162 – 173.

- [14] Dupuis, P., Grenander, U., Miller, M. I., 1998. Variational problems on flows of diffeomorphisms for image matching. *Quart. App. Math.* 56, 587–600.
- [15] Fletcher, T., Sep. 2011. Geodesic Regression on Riemannian Manifolds. In: *Proceedings of the Third International Workshop on Mathematical Foundations of Computational Anatomy - Geometrical and Statistical Methods for Modelling Biological Shape Variability*. pp. 75–86.
- [16] Goh, A., Lenglet, C., Thompson, P. M., Vidal, R., 2011. A nonparametric Riemannian framework for processing High Angular Resolution Diffusion Images and its applications to ODF-based morphometry. *NeuroImage*.
- [17] Goodlett, C. B., Fletcher, P. T., Gilmore, J. H., Gerig, G., 2009. Group analysis of dti fiber tract statistics with application to neurodevelopment. *NeuroImage* 45 (1, Supplement 1), S133 – S142.
URL <http://www.sciencedirect.com/science/article/pii/S1053811908011993>
- [18] Grenander, U., Miller, M. I., 1998. Computational anatomy: An emerging discipline. *Quart. App. Math.* 56 (4), 617–694.
- [19] Hinkle, J., Muralidharan, P., Fletcher, P. T., Joshi, S., Jan 2012. Polynomial regression on riemannian manifolds. *Tech. Rep.* arXiv:1201.2395.
- [20] Hua, K., Zhang, J., Wakana, S., Jiang, H., Li, X., Reich, D. S., Calabresi, P. A., Pekar, J. J., van Zijl, P. C., Mori, S., 2008. Tract probability maps in stereotaxic spaces: Analyses of white matter anatomy and tract-specific quantification. *NeuroImage* 39 (1), 336 – 347.
- [21] Huang, H., Ceritoglu, C., Li, X., Qiu, A., Miller, M. I., van Zijl, P. C., Mori, S., 2008. Correction of b0 susceptibility induced distortion in diffusion-weighted images using large-deformation diffeomorphic metric mapping. *Magnetic Resonance Imaging* 26, 1294–1302.
- [22] Huang, H., Zhang, J., Jiang, H., Wakana, S., Poetscher, L., Miller, M. I., van Zijl, P. C., Hillis, A. E., Wytik, R., Mori, S., 2005. DTI tractography based parcellation of white matter: Application to the mid-sagittal morphology of corpus callosum. *NeuroImage* 26 (1), 195 – 205.
- [23] Jenkinson, M., Smith, S., 2001. A global optimisation method for robust affine registration of brain images. *Med Image Anal* 5, 143–156.

- [24] Joshi, S. C., Davis, B., Jomier, M., Gerig, G., 2004. Unbiased diffeomorphic atlas construction for computational anatomy. *NeuroImage* 23, 151–160.
- [25] Lawes, I. N. C., Barrick, T. R., Murugam, V., Spierings, N., Evans, D. R., Song, M., Clark, C. A., 2008. Atlas-based segmentation of white matter tracts of the human brain using diffusion tensor tractography and comparison with classical dissection. *NeuroImage* 39 (1), 62 – 79.
- [26] Leergaard, T. B., White, N. S., de Crespigny, A., Bolstad, I., D’Arceuil, H., Bjaalie, J. G., Dale, A. M., 2010. Quantitative histological validation of diffusion MRI fiber orientation distributions in the rat brain. *PLoS One* 5, e8595.
- [27] Lim, K. O., Helpert, J. A., 2002. Neuropsychiatric applications of DTI - a review. *NMR in Biomedicine* 15 (7-8), 587–593.
- [28] Ma, J., Miller, M. I., Trouvé, A., Younes, L., 2008. Bayesian template estimation in computational anatomy. *NeuroImage* 42, 252–261.
- [29] Miller, M. I., Trouvé, A., Younes, L., 2006. Geodesic shooting for computational anatomy. *J. Mathematical Imaging and Vision* 24, 209–228.
- [30] Mori, S., Wakana, S., Lidia, van Zijl, P. C. M., 2010. *MRI Atlas of Human White Matter*, 2nd Edition. Elsevier.
- [31] Moseley, M., 2002. Diffusion tensor imaging and aging - a review. *NMR in Biomedicine* 15 (7-8), 553–560.
- [32] O’Donnell, L. J., Westin, C.-F., Golby, A. J., 2009. Tract-based morphometry for white matter group analysis. *NeuroImage* 45 (3), 832 – 844.
URL <http://www.sciencedirect.com/science/article/pii/S1053811908012822>
- [33] Park, H.-J., Kubicki, M., Shenton, M. E., Guimond, A., McCarley, R. W., Maier, S. E., Kikinis, R., Jolesz, F. A., Westin, C.-F., 2003. Spatial normalization of diffusion tensor mri using multiple channels. *NeuroImage* 20 (4), 1995 – 2009.
URL <http://www.sciencedirect.com/science/article/pii/S1053811903004981>
- [34] Qiu, A., Brown, T., Fischl, B., Ma, J., Miller, M. I., 2010. Atlas generation for subcortical and ventricular structures with its applications in shape analysis. *IEEE Transactions on Image Processing* 19 (6), 1539–1547.

- [35] Qiu, A., Oishi, K., Miller, M. I., Lyketsos, C. G., Mori, S., Albert, M., 03 2010. Surface-based analysis on shape and fractional anisotropy of white matter tracts in alzheimer's disease. *PLoS ONE* 5, e9811.
- [36] Rao, C. R., 1945. Information and accuracy attainable in the estimation of statistical parameters. *Bull. Calcutta Math Soc.* 37, 81–89.
- [37] Srivastava, A., Jermyn, I., Joshi, S. H., 2007. Riemannian analysis of probability density functions with applications in vision. In: *IEEE CVPR*.
- [38] Sullivan, E., Pfefferbaum, A., Adalsteinsson, E., Swan, G., Carmelli, D., 2002. Differential rates of regional brain change in callosal and ventricular size: a 4-year longitudinal MRI study of elderly men. *Cerebral Cortex* 12 (4), 438–445.
- [39] Tao, X., Miller, J. V., 2006. A method for registering diffusion weighted magnetic resonance images. In: *MICCAI*. pp. 594–602.
- [40] Trouvé, A., 1998. Diffeomorphism groups and pattern matching in image analysis. *Int. J. of Comp. Vis.* 28 (3), 213–221.
- [41] Tuch, D. S., 2002. High angular resolution diffusion imaging reveals intravoxel white matter fiber heterogeneity. *MRM* 48, 577–582.
- [42] Verhoeven, J. S., Sage, C. A., Leemans, A., Van Hecke, W., Callaert, D., Peeters, R., De Cock, P., Lagae, L., Sunaert, S., 2010. Construction of a stereotaxic DTI atlas with full diffusion tensor information for studying white matter maturation from childhood to adolescence using tractography-based segmentations. *Human Brain Mapping* 31 (3), 470–486.
- [43] Yeh, F.-C., Tseng, W.-Y. I., 2011. NTU-90: A high angular resolution brain atlas constructed by q-space diffeomorphic reconstruction. *NeuroImage* 58 (1), 91 – 99.
- [44] Yushkevich, P. A., Zhang, H., Simon, T. J., Gee, J. C., 2008. Structure-specific statistical mapping of white matter tracts. *NeuroImage* 41 (2), 448 – 461.
URL <http://www.sciencedirect.com/science/article/pii/S1053811908000323>
- [45] Zhang, H., Yushkevich, P. A., Rueckert, D., Gee, J. C., 2007. Unbiased white matter atlas construction using diffusion tensor images. In: *Proceedings of the 10th international conference on Medical image computing and computer-assisted intervention. MICCAI'07. Springer-Verlag, Berlin, Heidelberg*, pp. 211–218.
URL <http://dl.acm.org/citation.cfm?id=1775835.1775865>